

The role of inhibition in oscillatory wave dynamics in the cortex

Ying Xiao,¹ Xiao-ying Huang,² Stephen Van Wert,¹ Ernest Barreto,³ Jian-young Wu,² Bruce J. Gluckman¹ and Steven J. Schiff^{1,4,*}

¹Center for Neural Engineering, Department of Engineering Science and Mechanics, Pennsylvania State University, University Park, PA, USA

²Department of Physiology and Biophysics, Georgetown University Medical Center, Washington, DC, USA

³School of Physics, Astronomy, and Computational Sciences, The Center for Neural Dynamics and The Krasnow Institute for Advanced Study, George Mason University, Fairfax, VA, USA

⁴Department of Neurosurgery and Department of Physics, Pennsylvania State University, University Park, PA, USA

Keywords: brain oscillation, complexity, dimension, frequency, rat, synchronization

Abstract

Cortical oscillations arise during behavioral and mental tasks, and all temporal oscillations have particular spatial patterns. Studying the mechanisms that generate and modulate the spatiotemporal characteristics of oscillations is important for understanding neural information processing and the signs and symptoms of dynamical diseases of the brain. Nevertheless, it remains unclear how GABAergic inhibition modulates these oscillation dynamics. Using voltage-sensitive dye imaging, pharmacological methods, and tangentially cut occipital neocortical brain slices (including layers 3–5) of Sprague-Dawley rat, we found that GABA_A disinhibition with bicuculline can progressively simplify oscillation dynamics in the presence of carbachol in a concentration-dependent manner. Additionally, GABA_B disinhibition can further simplify oscillation dynamics after GABA_A receptors are blocked. Both GABA_A and GABA_B disinhibition increase the synchronization of the neural network. Theta frequency (5–15-Hz) oscillations are reliably generated by using a combination of GABA_A and GABA_B antagonists alone. These theta oscillations have basic spatiotemporal patterns similar to those generated by carbachol/bicuculline. These results are illustrative of how GABAergic inhibition increases the complexity of patterns of activity and contributes to the regulation of the cortex.

Introduction

Brain oscillations are widely observed, including in the olfactory system (Lepousez *et al.*, 2010), visual (Edden *et al.*, 2009; Sun & Dan, 2009), sensorimotor (Reimer & Hatsopoulos, 2010), auditory system (Luo & Poeppel, 2007) and hippocampus (Buzsáki, 2002; Geisler *et al.*, 2010). In the neocortex, oscillations occur at rest (Arieli *et al.*, 1996; Mak & Wolpaw, 2009), and during spatial learning and working memory (Raghavachari *et al.*, 2001; Rizzuto *et al.*, 2003). Oscillations are important in spreading depression (Koroleva *et al.*, 2009), migraine (Coppola *et al.*, 2005), seizures (Worrell *et al.*, 2004), and Parkinson's disease (Schiff, 2010).

Oscillations are organized into spatiotemporal patterns, and patterns may propagate as traveling waves. Oscillatory traveling waves have been observed in the olfactory bulb (Lam *et al.*, 2000), motor cortex (Rubino *et al.*, 2006), visual cortex (Xu *et al.*, 2007), and spiral waves during sleep (Huang *et al.*, 2010). Propagating waves of activity occur in epilepsy (Telfeian & Connors, 1998). The physiological role of

traveling spatiotemporal oscillatory waves remains speculative (Ermentrout & Kleinfeld, 2001).

In vitro brain slices are useful for studying the mechanisms of oscillatory waves. Slice oscillations occur spontaneously in normal artificial cerebrospinal fluid (ACSF) (Wu *et al.*, 2001). Theta frequency oscillations (4–15 Hz in rodents) can be generated in slices by cholinergic activation using carbachol with (Lukatch & MacIver, 1997; Bao & Wu, 2003; Cappaert *et al.*, 2009) or without (Fisahn *et al.*, 1998; Pálhalmi *et al.*, 2004) GABAergic disinhibition, and also employing 4-aminopyridine (Tancredi *et al.*, 2000), high potassium (Towers *et al.*, 2002) or low magnesium (Flint *et al.*, 1997; Ziburkus *et al.*, 2006).

Active inhibition limits the spread of epileptiform activity (Treiman, 2001; Richter *et al.*, 2010). Oscillations in disinhibited tissues are associated with increased firing rates (Sanchez-Vives & McCormick, 2000), and true spiral waves are seen (Huang *et al.*, 2004). The role of GABA_B inhibition remains unclear (Buzsáki, 2002; De la Prida *et al.*, 2006). We are aware of no systematic titration of the strength of inhibition with respect to the spatiotemporal dynamic characteristics of oscillatory cortical waves.

The dynamics of neuron populations can be observed with voltage-sensitive dye (VSD) imaging *in vitro* (Yuste *et al.*, 1997; Bai *et al.*, 2006; Carlson & Coulter, 2008) and *in vivo* (Precht *et al.*, 1997; Xu

Correspondence: Steven J. Schiff, *present address below.
E-mail: sschiff@psu.edu

*Present address: W311 Millennium Science Complex, The Pennsylvania State University, University Park, PA 16802, USA

Received 19 December 2011, revised 20 March 2012, accepted 23 March 2012

et al., 2007; Palagina *et al.*, 2009; Huang *et al.*, 2010). Unidirectional propagating waves (4–15 Hz theta) in coronal cortical slices have a quasi one-dimension character (Wu *et al.*, 2001; Bao & Wu, 2003). However, in tangential slices, oscillations can propagate as complex two-dimensional waves (Huang *et al.*, 2004). Four basic types of patterns in tangential slices are observed (Huang *et al.*, 2004): irregular, plane, ring and spiral. Tangential slices preserve more of the natural dynamics of oscillations than coronal slices where oscillatory dynamics are more constrained.

Here we examine the effects of inhibition and excitation on two-dimensional cortical wave dynamics with VSD imaging. We find increased complexity as inhibition increases, and demonstrate that a combination of pure disinhibitory GABA_A and GABA_B blockade permits robust oscillatory traveling wave formation without muscarinic activation.

Materials and methods

Tangential cortical slice preparation

All experiments were performed with approval from the Institutional Animal Care and Use Committee of Penn State University. Neocortical slices were obtained from 27 male Sprague-Dawley rats from postnatal day 21 to 35. The animals were deeply anesthetised with diethyl-ether and decapitated. The whole brain was quickly removed and chilled in cold (4 °C) ACSF [containing the following (in mM): 132 NaCl, 3 KCl, 2 CaCl₂, 2 MgSO₄, 1.25 NaH₂PO₄, 26 NaHCO₃, and 10 dextrose] for 60 s. The ACSF was saturated with 95% O₂ and 5% CO₂ at room temperature for 1 h before the experiment. Tangential slices were cut, according to Huang *et al.* (2004), with a vibratome on the rostrocaudal and mediolateral coordinates of bregma –2 to –8 mm and lateral 1–6 mm, respectively. The first cut was made 300 μm deep from the pial surface, and the tissue was discarded. The second cut was made 500 μm deeper to obtain a 500-μm-thick slice of the middle cortical layers (including layers 3–5) (Huang *et al.*, 2004). The 500-μm-thick slice was transferred into a holding chamber containing ACSF and incubated at 26 °C for at least 1 h before staining. After 2 h staining and 0.5 h recovering in ACSF, the slice was transferred to a submersion chamber. The slice was perfused with ACSF at a rate of > 20 mL/min for 30 min (30–31 °C) in the chamber before recording. Because of the curvature of the cortex, the size of the tangential slices was limited to about 5 × 6 mm². The anatomical regions included in these slices included the primary and secondary visual cortex within the field of view imaged, with portions of the primary somatosensory and parietal association cortices lying outside the field of view. Layer 5 was facing up in all the experiments and the slices in all the figures were oriented in the same way. The location of the stimulation electrode was kept consistent for the same slice in different experiments. The stimulus amplitude was chosen to be 1 mA above the threshold amplitude for oscillation generation and kept consistent for the same slice for different drug conditions.

Voltage-sensitive dye imaging

The imaging apparatus and methods are described in detail in Jin *et al.* (2002). Briefly, slices were stained for 2 h with 5 μg/mL of an absorbance oxonol dye, NK3630 (Nippon Kankoh-Shikiso Kenkyusho, Okayama, Japan). The dye was dissolved in ACSF (26 °C) on the day of use. VSD images were taken by a 464-element photodiode array (WuTech Instruments) with 1.6-kHz sampling rate. An objective of 4× (0.10 NA, dry lens; Zeiss) was used to project the image of the

tissue to the diode array and each photo detector received light from an area of 0.41 × 0.41 mm² of the tissue. The preparation was transilluminated by 705 ± 20-nm light and was only exposed to the illumination light during optical recording trials for about 10 s/trial. The typical voltage-sensitive signal was 10⁻³–10⁻⁵ of the resting light intensity.

Pharmacological agents

Carbamylcholine chloride (carbachol), (–)-bicuculline methiodide (Biomol[®]), picrotoxin, 6-cyano-7-nitroquinoxaline-2,3-dione (CNQX), 2,3-dioxo-6-nitro-1,2,3,4-tetrahydrobenzo[f]quinoxaline-7-sulfonamide (NBQX), D-(–)-2-amino-5-phosphonopentanoic acid (D-APV), dimethyl sulfoxide (DMSO) and 3-[(3,4-dichlorophenyl)methyl]aminopropyl (diethoxymethyl) phosphinic acid (CGP52432) were used in combinations to evoke or suppress oscillations. Carbachol, bicuculline, CGP52432 and D-APV were made into high-concentration stock solutions with deionised water (18 MΩ resistance). Picrotoxin, CNQX and NBQX were dissolved in DMSO. The final concentration of DMSO was 0.05% (v/v) when picrotoxin was added into the solution, and 0.1% (v/v) when CNQX or NBQX was added. As reported in Fink *et al.* (2000), these final concentrations of DMSO did not appear to affect our experiments. Carbachol, picrotoxin and DMSO were purchased from Sigma-Aldrich (St Louis, MO, USA). CNQX, NBQX, D-APV and CGP52432 were purchased from Tocris (Ellisville, MO, USA).

Data analysis

Data visualization and dynamics analysis

The optical data were acquired using NEUROPLEX software (Red-ShirtImaging, Fairfield, CT, USA). Oscillations from each slice were evoked by a 0.5 ms 5–7 mA square-wave pulse, and further analysed using MATLAB programs (Mathworks, Natick, MA, USA). In brief, raw data acquired at 1.6 kHz were resampled to 1000 Hz. There is a 0.5–1.0 s latent period following brief stimulation when inducing such wave patterns, which, to our knowledge, has not yet been characterised. To remove the initial stimulus artifact and coupled neuronal activation, as well as the latent period, the first 2 s of resampled data were discarded. (We illustrate examples of the initial stimulation and latent period in Supporting Information Figs S1, S2, and S3.) The remaining data were normalised by the maximum value from each photodiode signal; the normalised data were low-pass filtered under 30 Hz for spectral coherency analysis (described below). Based on the results from spectral coherency analysis, the normalised data were further band-pass filtered between 5 and 30 Hz for synchrony and dynamics analysis to focus on results as free of artifact as possible. In Supporting Information Figs S1, S2, and S3, we included frequencies of 0–5 Hz in both optical and electrical signals, and the correlated low frequencies in optical tracings can clearly be seen in contrast with the electrical signal. At 705 nm, one can see the intrinsic optical signal related to cell swelling in the optical measurements but, at this light frequency, the intrinsic signal will not mask the neuronal voltage signal (Bai *et al.*, 2006). Furthermore, the intrinsic optical signal tends to correlated with and lag behind neuronal activity, features not clearly represented in our low-frequency traces. We therefore attribute most of our optically-only correlated optical signal to movement artifact, which is corroborated by the spectra in the Supporting Information figures demonstrating no difference in frequencies below 5 Hz in the different experimental conditions that affect the neuronal activity of

these slices. Spectral analysis was performed using a multitaper method (Mitra & Pesaran, 1999). As the presence of shot-noise in the optical signal makes direct visualization of the space-time data difficult, filtered data were further spatiotemporally denoised using singular value decomposition (Mitra & Pesaran, 1999; Schiff *et al.*, 2007).

The activity patterns of denoised data were obtained by visualizing the full sequence of images displayed as pseudocolor images. In the pseudocolor images, data from each optical detector were normalised to their own maximum, and then each normalised data point was assigned a color according to a linear color scale. Therefore, the smallest normalised data point was assigned zero on the color scale and showed deep blue in the image; the maximum normalised data point was assigned 1 on the color scale and showed deep red. Displayed figures were further smoothed with a 3×3 spatial filter. The complexity of wave dynamics was quantified by a modal dimension analysis (Schiff *et al.*, 2007). A one-tailed *t*-test was used to determine the significance level of differences between two groups. One-way ANOVA and Tukey *post hoc* testing were used to determine the significance level of differences between more than two groups. $P < 0.05$ was regarded as significant.

Bootstrap method

In the present study, bootstrapping was based on resampling time series multiple times by exchanging segments of a time series at a different random location (see detailed description in Schiff *et al.*, 2005). The resultant surrogate data sets are measured in the same way as the original data to generate an ensemble of measurements. For the surrogate data sets, the local correlations are largely destroyed. Only the values above the 95th percentile of the ensemble of measurements obtained from the surrogate data sets will be considered meaningful.

Spectral coherency analysis

In VSD measurements from brain slices, there are artifacts caused by vibrations and fluid waves in the light path. Motion artifacts in the VSD signal should have no relationship with the membrane potential changes of interest. In order to study neural activity without the contamination of vibration artifacts, the signal frequency range of interest for analysis was determined through a comparative coherency analysis.

We consider that signals coherent in frequency (or significantly correlated in the time domain) in both local field potential (LFP) and optical signals are electrical signals that are caused by membrane potential changes. If the signal in some frequency band is only coherent between optical detectors but not coherent in LFP at the same time, this signal is likely to be an artifact. It is also possible that the optical signals are correlated by slow intrinsic optical signals (Bai *et al.*, 2006), which would not be relevant to the present study. In brief, the LFP and signals from four optical detectors (labeled optical 1, optical 2, optical 3 and optical 4), which were spatially close to the tip of the LFP recording electrode, were chosen for each trial to perform the coherency analysis. The LFP and optical signals were resampled to 1000 Hz and low-pass filtered at 30 Hz before calculating the multitaper normalised cross-spectrum for each pair of filtered data from two optical detectors (data pairs include: optical 1–optical 2, optical 1–optical 3, optical 1–optical 4, optical 2–optical 3, optical 2–optical 4, optical 3–optical 4) or from the data pair of LFP and one optical detector (data pairs include: LFP–optical 1, LFP–optical 2, LFP–optical 3, LFP–optical 4). These 10 data pairs were analysed for each trial. The bootstrap method was used to set the statistical reference for the confidence level. For each data set (LFP or

optical), the time series within each 6-s window was resampled 1000 times by bootstrapping. The surrogate data pairs were subjected to the same multitaper coherency analysis and the same 95th percentile confidence level was used as with the original data pair. To be very conservative, only coherency levels of the original data pair greater than the bootstrapped 95th percentile were considered likely to be significant.

In Fig. 1, most of the coherent frequencies between the LFP and optical signals (shown as blue circles) were within the range of 5–30 Hz, whereas most of the coherent frequencies between optical signals alone (shown as red circles) were within the 0–5 Hz range. When optical–optical signals were coherent within the 5–30 Hz range, they all closely overlapped with coherent frequencies between LFP and optical signals. Therefore, coherent frequencies within the 5–30 Hz band appear largely artifact free and reflect membrane potential changes. The situation below 5 Hz is considerably more complex. As shown in Fig. 1, there are examples where the optical–optical coherency is confirmed by the optical–LFP coherency, and many examples where the optical–optical and LFP–optical coherencies are separate. To be conservative, we will eliminate from study in this report all of the coherent results within this lower frequency range, recognizing that in this process we will eliminate some very real low-frequency correlations that are present in our measurements. Based on these screening coherencies, we therefore band-pass filtered all data between 5 and 30 Hz to focus on describing results as free of artifact as possible.

Synchrony analysis

Synchrony analysis was performed according to the methods described in Schiff *et al.* (2005; a code archive is available with this citation). For computational efficiency, signals from 31 optical detectors were selected, so that the picked detectors were distributed in the imaging field as evenly as possible. The sampled detectors were the same for each experiment. Cross-correlation at both zero lag and arbitrary lags, and phase variance for all data pairs, were calculated for

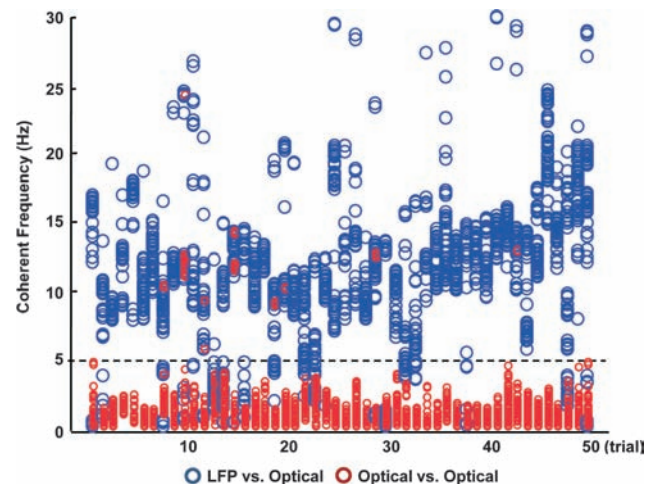


FIG. 1. Spectral coherency analysis. Each column of markers represents the coherency analysis of a 6-s oscillation episode in each of 50 trials from different slices. The oscillations were generated using six pharmacological combinations with the trigger of a 0.5-ms 5–7 mA single square-wave electrical pulse. The pool of the coherent (or significantly correlated) frequencies derived from four pairs of LFP–optical data for one trial are shown in one column using blue circles; the red circles shown in the same column represent the coherent frequencies derived from six pairs of optical–optical data for the same trial. Note that red and blue circles above 5 Hz overlap within narrow frequency ranges.

each non-overlapping 1-s window of 5–30 Hz filtered data. For phase variance, phase was assigned from Hilbert transformation of each 6 s time series from each optical detector using the method of Bendat & Piersol (1986). For each time point of the 6 s trial, the sum of the cosine and the sum of the sine of the phases over all the 31 optical detectors were taken, and the average phase angle was calculated for each time point. The sequential average angle was unwrapped before calculating the difference between adjacent average angles. The variance of the differences between sequential average angles was calculated for each 1 s time window to generate the phase variance.

Bootstrapping was used to obtain the statistical confidence level of cross-correlation at zero and arbitrary lags as well as the phase variance. Data were resampled 100 times within each non-overlapping 1 s window. The cross-correlation at zero lag for each second was considered significant when its value was above the 95th percentile of the ensemble of cross-correlation obtained from the surrogate data sets. The mean value and SD of the ensemble of the cross-correlation value can be calculated and the mean \pm twice the SD was taken as the confidence interval; only the cross-correlation values at arbitrary lag beyond the confidence interval were considered significant and their absolute value summed. The phase variance for each second was considered significant when the value was smaller than the 5th percentile of the ensemble of bootstrapped phase variance. The sum of cross-correlation at zero lag for the whole 6 s duration window for all data pairs was also calculated by summing the significant cross-correlation at zero lag from each second of data. The sum of cross-correlation at arbitrary lags for the whole 6 s window for all data pairs

was calculated by summing the significant cross-correlation at arbitrary lags from each second of data. The sum of phase variance for the whole 6 s duration window was calculated by summing the significant phase variance from six 1 s windows. The sum of cross-correlation at both zero lag and arbitrary lags and sum of phase variance were normalised before they were compared using a one-tailed *t*-test or ANOVA.

Results

Effects of GABA_A receptor, GABA_B receptor, N-methyl-D-aspartate receptor and AMPA receptor blockade on oscillation waveforms

In the following GABA_A titration experiments, 100 μ M carbachol was used in the perfusate to activate the slices (after Huang *et al.*, 2004). The bicuculline concentration was increased gradually from 1 to 10 μ M. Although oscillatory episodes will occur spontaneously in disinhibited transverse cortical slices, we typically used small electrical stimuli to trigger such events in order to reduce exposure to phototoxic effects with VSD imaging (Huang *et al.*, 2004). Without bicuculline in the perfusate, propagating oscillations could not be evoked by a single electrical pulse stimulus. With 1 μ M bicuculline, low-amplitude propagating theta frequency oscillations were evoked (Fig. 2B). The beginning second or so of the trace in Fig. 2B shows an irregular waveform, followed by more regular oscillations as the episode evolves (a more complete discussion of such event evolution can be found in Schiff *et al.*, 2007). When bicuculline was increased to 5 or 10 μ M, propagating theta

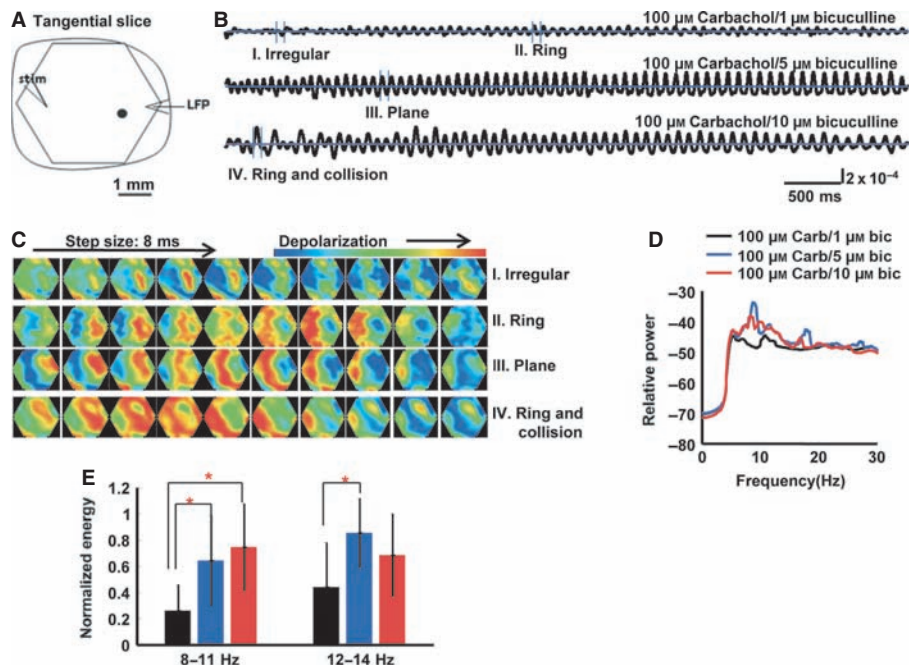


FIG. 2. Results for bicuculline titration experiments. (A) Schematic drawing of the imaging field (hexagonal) with a $4\times$ objective overlying a $500\text{-}\mu\text{m}$ -thick tangential occipital cortical slice. The slice included layers 3–5. A $0.5\text{ ms } 6\text{ mA}$ single square-wave electrical pulse was given at the edge of the slice as a stimulus (stim) to evoke oscillations. The LFP at the edge of the slice was recorded simultaneously with the optical recordings. One example optical detector is indicated as a black filled circle within the imaging field. Data from optical detectors that are spatially close to the LFP recording electrode tip are needed to obtain filter criteria by coherency analysis before further analyses, whereas traces from optical detectors used to accompany the pseudocolor images are not required to be close to the LFP recording electrode tip. Signals measured at the picked detector are shown as 6 s traces in B. The blue lines in traces of B are zero baselines. Vertical scale: 2×10^{-4} of resting light intensity. (C) Four sections from the temporal data (I–IV) in B are displayed as a sequence of pseudocolor images. These pseudocolor images are displayed at 8 ms intervals between frames. In the images, warmer colors represent increasing depolarization. (D) Power spectrum (logarithmic scale) for optical signals during a 6 s episode averaged across all detectors of 10 slice experiments. Carb, carbachol; bic, bicuculline. (E) Bar plot shows the average normalised energy in two frequency ranges corresponding to three bicuculline concentrations. Error bars represent \pm SD. Black, blue and red bars represent 1, 5 and 10 μ M bicuculline, respectively. The 10 μ M bicuculline group had significantly higher energy at 8–11 Hz than the 1 μ M bicuculline group, whereas the 5 μ M bicuculline group had significantly higher energy at 8–11 and 12–14 Hz than the 1 μ M bicuculline group. The significant differences between groups in E are marked by asterisks.

frequency oscillations showed higher amplitudes and more regular waveforms (Fig. 2B). Power spectrum analysis was performed on the oscillations generated by different bicuculline concentrations and the energy of frequency components was compared between groups. When bicuculline was increased from 1 to 5 μM , the dominant frequency peak in the average power spectrum of 10 slices shifted towards a lower frequency (from 10 to 8 Hz); when bicuculline increased to 10 μM , the frequency peak continued its drift towards a lower frequency (Fig. 2D). Statistical analyses (one-way ANOVA and Tukey *post hoc* testing) confirmed that, when bicuculline was increased from 1 to 5 μM , the energy of the 8–11 and 12–14 Hz frequency components of 10 slices was significantly increased ($df = 29$, $F = 6.25$, $P = 0.0059$ and $df = 29$, $F = 4.52$, $P = 0.0203$, respectively) (Fig. 2E), and the energy of the 8–11 Hz ($df = 29$, $F = 6.25$, $P = 0.0059$) frequency components was significantly increased by 10 μM bicuculline compared with 1 μM bicuculline (Fig. 2E).

The GABA_B antagonist CGP52432 was applied to examine the influence of GABA_B on theta frequency oscillation. Compared with

those evoked without CGP52432, the oscillation waveform became more regular with 100 μM carbachol/10 μM bicuculline/4 μM CGP52432 (compare traces in Fig. 3B). These results are consistent with the increased oscillation amplitude shown for a similar drug combination in Lukatch & MacIver (1997), although they did not discuss these displayed findings. The dominant frequency peak in the average power spectrum of nine slices shifted from 12 to 7 Hz when compared with the group without CGP52432 (Fig. 3C). The energy of the 5–9 Hz (one-tailed *t*-test, $df = 16$, $P = 6.74 \times 10^{-6}$), 11–17 Hz ($df = 16$, $P = 0.0015$), 22–23 Hz ($df = 16$, $P = 0.0396$) and 25–26 Hz ($df = 16$, $P = 0.0235$) frequency components was significantly increased by CGP52432 (Fig. 3D).

Consistent with coronal neocortical slices (Lukatch & MacIver, 1997), blocking *N*-methyl-D-aspartate (NMDA) receptors using 80 μM D-APV generated the appearance of large-amplitude irregular waves in place of more rhythmic ones (compare traces in Fig. 3E). D-APV altered the frequency content of the oscillations (Fig. 3F), with the energy of the 10–11-Hz components of eight slices significantly

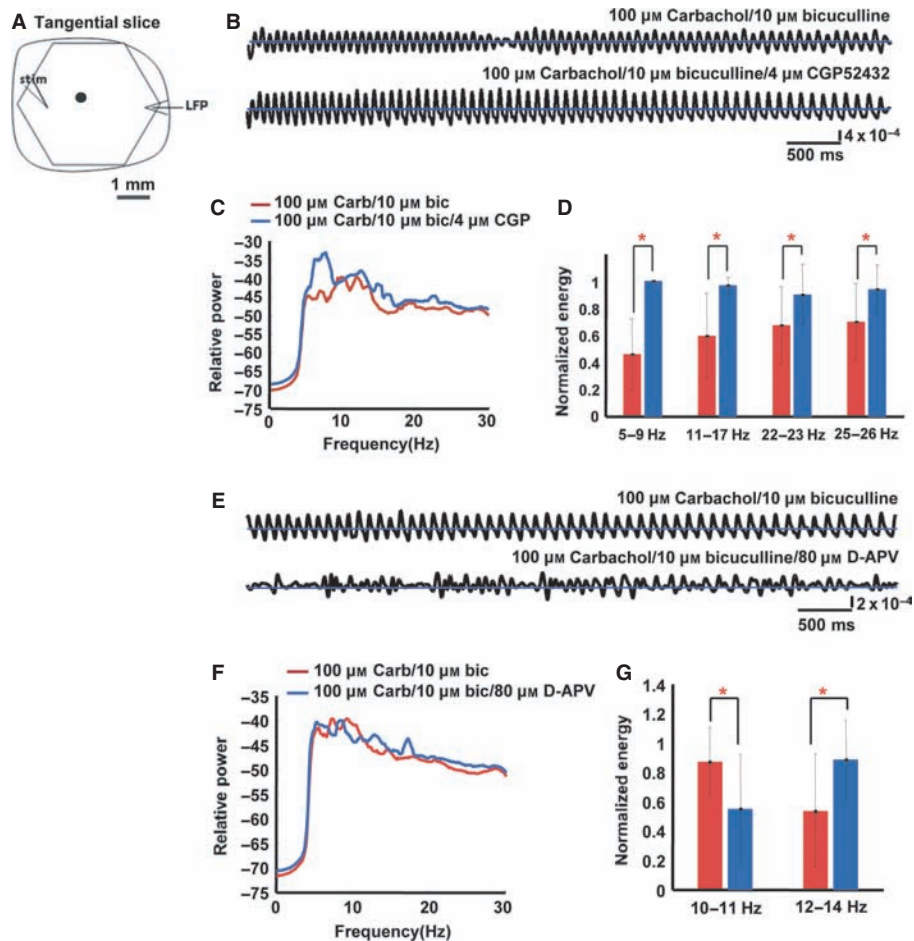


FIG. 3. The effects of GABA_B disinhibition and NMDA receptor blockade on theta oscillation waveforms. (A) Recording arrangement, with stimulation (stim) and local field potential (LFP) electrodes. Signals from one example optical detector (marked as a black filled circle in A) with and without GABA_B inhibition are shown as 6 s traces in B. Traces in E are signals from the same example optical detector with and without NMDA receptor activation. The blue lines in traces of B and E are zero baselines. In B, vertical scale: 4×10^{-4} of resting light intensity; in E, vertical scale: 2×10^{-4} of resting light intensity. (C) Power spectrum (logarithmic scale) for the optical signals during a 6 s episode, averaged across all detectors from nine slice experiments. Carb, carbachol; bic, bicuculline; CGP, CGP52432. The average peak frequencies with 100 μM carbachol/10 μM bicuculline were about 10 and 12 Hz. When CGP52432 was in the solution, the peak was about 7 Hz with a more minor peak at about 12 Hz. (D) Bar plot shows the average normalised energy in four frequency ranges corresponding to conditions with and without GABA_B inhibition. Error bars represent \pm SD. Red and blue bars represent the 100 μM carbachol/10 μM bicuculline group and the 100 μM carbachol/10 μM bicuculline/4 μM CGP52432 group, respectively. CGP52432 significantly elevated energy at 5–9, 11–17, 22–23 and 25–26 Hz when compared with the group without CGP52432. (F) Power spectrum for conditions with and without NMDA receptor activation, averaged across all detectors from eight slice experiments. (G) Energy analysis. Red and blue bars represent the 100 μM carbachol/10 μM bicuculline group and the 100 μM carbachol/10 μM bicuculline/80 μM D-APV group, respectively. D-APV significantly decreased energy at 10–11 Hz and significantly increased energy at 12–14 Hz when compared with the no D-APV group. The significant differences between groups in D and G are marked by asterisks.

(one-tailed *t*-test, $df = 14$, $P = 0.0289$) decreased by D-APV, whereas the energy of the 12–14-Hz components was significantly ($df = 14$, $P = 0.0276$) increased (Fig. 3G).

Similar to coronal neocortical slice results (Lukatch & MacIver, 1997), propagating oscillations in tangential occipital neocortical slices also required AMPA receptor-mediated synaptic transmission. When AMPA receptors were blocked with 30 μM CNQX (NBQX), which was also used in the present study, had very similar effects on these oscillations as CNQX, propagating oscillations were eliminated (Supporting Information Fig. S4).

Effects of GABA_A and GABA_B disinhibition, and N-methyl-D-aspartate blockade on oscillation dynamics

Each temporal oscillation cycle was associated with one spatial propagating wave (consistent with Bao & Wu, 2003). The spatiotemporal pattern of one propagating wave can be observed by visually inspecting sequential pseudocolor images. In general, the wave patterns can be classified as regular waves and irregular waves. Regular waves are defined as the waves that repeatedly appear in a certain pattern for several cycles of an oscillation episode. Simple regular waves include three basic patterns: ring waves (such as the image in Fig. 2CII, and Supporting Information movie file M1), plane waves (such as the images in Fig. 2CIII, and Supporting Information movie file M2) and spiral waves (such as the images in Fig. 6DIV, and Supporting Information movie file M3). In addition to simple basic patterns, regular waves in the present study also included complex patterns, which were the combination of one or more basic wave patterns, such as ring with collision (Fig. 2CIV, and Supporting Information movie file M4), multiple rings (Fig. 6DIII), etc. Irregular waves change pattern from cycle to cycle and are not periodic.

The changes in complexity of oscillation dynamics can be visualised by the use of trajectory plots of modal amplitudes (Schiff *et al.*, 2007). These modal amplitudes are the amplitudes of the spatial modes calculated from a singular value decomposition, and these trajectory plots have been employed as a means of visualizing wave data from both whole-brain (Senseman & Robbins, 1999) and slice data (Schiff *et al.*, 2007). Simple periodic dynamics tend to show closed loops or limit-cycles when plotted in this manner. When the spatiotemporal dynamics are complex (substantially greater than three dimensions), and aperiodic, the trajectory plots tend to show a lack of organised structure. Trajectory plots revealed that oscillations evoked with 5 and 10 μM bicuculline had much simpler dynamics than those evoked with 1 μM bicuculline (compare the three rows of trajectory plots in Fig. 4A). Analysis for 10 slices showed that oscillations evoked with 5 and 10 μM bicuculline had significantly lower dimension in spatial-frequency ($df = 29$, $F = 12.07$, $P = 0.0002$) and spatial-amplitude ($df = 29$, $F = 11.17$, $P = 0.0003$) modes than those evoked with 1 μM bicuculline (Fig. 4B). The dynamics of oscillations evoked by 100 μM carbachol/10 μM bicuculline was further simplified by 4 μM CGP52432 (Fig. 4C). Dimension analysis for nine slices confirmed that CGP52432 significantly decreased the dimension of oscillations in both spatial-frequency (one-tailed *t*-test, $df = 16$, $P = 0.0083$) and spatial-amplitude ($df = 16$, $P = 0.0152$) modes when compared with the group without CGP52432 (Fig. 4D). However, NMDA blockade by 80 μM D-APV complicated the dynamics of oscillations evoked by 100 μM carbachol/10 μM bicuculline (Fig. 4E). Dimension analysis for eight slices confirmed that D-APV significantly increased dimension of oscillations in both spatial-frequency ($df = 14$, $P = 0.0022$) and spatial-amplitude ($df = 14$, $P = 0.0447$) modes (Fig. 4F).

In summary, in the presence of carbachol, GABA_A, and GABA_B disinhibition, there was a significant decrease in the dynamical

complexity of oscillations, whereas NMDA blockade significantly increased the dynamical complexity.

Modulation of neural response synchronization by GABA_A and GABA_B disinhibition, and N-methyl-D-aspartate blockade

The synchronization of neural responses was measured by three parameters: the cross-correlation sum at zero lag, cross-correlation sum at arbitrary lags, and sum of phase variance. The average results of 10 slices for the modulation of synchrony by GABA_A disinhibition are shown in Fig. 5A. There was no significant change in the cross-correlation sum at zero lag. However, 10 μM bicuculline significantly increased the cross-correlation sum at arbitrary lags when compared with 1 μM bicuculline (ANOVA and Tukey *post hoc* analysis, $df = 29$, $F = 5.23$, $P = 0.012$); 5 and 10 μM bicuculline also significantly decreased the sum of phase variance, reflecting increased synchronization ($df = 29$, $F = 4.07$, $P = 0.0285$) when compared with 1 μM bicuculline. Phase can be a useful metric of synchronization in non-linear systems when linear cross-correlation may be insensitive (Pikovsky *et al.*, 2000). However, this issue is complex (Netoff *et al.*, 2004) and we present both types of measurement here to more fully capture the characteristics of the interactions of these neuronal networks.

The average results of nine slices for the modulation of synchrony by GABA_B disinhibition are shown in Fig. 5B. The cross-correlation sums at both zero lag and arbitrary lags were significantly higher (one-tailed *t*-test, $df = 16$, $P = 0.0018$ and $df = 16$, $P = 0.0081$, respectively) with 100 μM carbachol/10 μM bicuculline/4 μM CGP52432 than without CGP52432. However, the sum of phase variance was not significantly changed when CGP52432 was added into the perfusate. There was no significant change in synchronization in the presence of NMDA receptor blockade (Fig. 5C).

In summary, there appeared to be an increase in both cross-correlation and phase synchronization with GABA_A disinhibition, and a further increase in cross-correlation with GABA_B disinhibition.

Oscillations and spatiotemporal patterns evoked by picrotoxin/CGP52432

Might GABA modulation alone be sufficient to generate propagating oscillations? We found that bicuculline alone was insufficient to produce wave oscillations (data not shown). To focus on GABA modulation, we note that bicuculline not only competitively blocks GABA_A receptors, but also blocks the apamin-sensitive small-conductance Ca-activated K⁺ channel (SK channel) (Kleiman-Weiner *et al.*, 2009). Picrotoxin, which has no known action on the SK channel (Debarbieux *et al.*, 1998), was therefore introduced as a more selective GABA_A blocker without the confounding effects of SK channel blockade. It was found that 6 μM CGP52432 and picrotoxin [50 μM , equally effective as 10 μM bicuculline in blocking GABA_A receptor-mediated inhibition (Pisani *et al.*, 2002)] reliably evoked theta oscillations in seven out of seven slices (Fig. 6B). The dominant peak frequencies of the average power spectrum were 6 and 11 Hz (Fig. 6C). All the basic wave patterns (spiral, plane, ring, irregular waves) generated by carbachol/bicuculline could be observed in experiments with 50 μM picrotoxin/6 μM CGP52432 (Fig. 6D).

Discussion

The present study found that propagating theta oscillations in tangential occipital neocortical slices were based on AMPA receptor-mediated synaptic transmission. GABAergic inhibition affected both

the dynamical complexity of oscillations and synchronization. Blockade of GABAergic inhibition significantly simplified oscillatory dynamics. The blockade of NMDA receptors significantly complicated oscillation dynamics. Both GABA_A and GABA_B disinhibition altered the synchronization of the spatial patterns in different ways. Blockade of GABA_A and GABA_B with picrotoxin/CGP52432 reliably generated propagating theta oscillations that shared many of the characteristics of waves generated with carbachol/bicuculline.

Comparison with other studies

Oscillations in the brain can be evoked in many ways. In human neocortical, rat hippocampal, and rat coronal neocortical slices, oscillations evoked by bicuculline, carbachol, or their combination depend primarily on non-NMDA excitatory amino acids (MacVicar & Tse, 1989; McCormick, 1989; Lukatch & MacIver, 1997; Williams & Kauer, 1997). The present study confirmed that oscillations evoked by carbachol/bicuculline in rat tangential occipital neocortical slices were

eliminated by AMPA receptor antagonists but could not be eliminated by either NMDA antagonists or GABA antagonists.

Although it has been reported that GABA_A receptor-mediated inhibition has no clear effect on carbachol-evoked theta oscillation in rat hippocampal slices (MacVicar & Tse, 1989), the titration of bicuculline in the present study slowed the peak frequency and increased the amplitude of oscillations. This result appears consistent with the shortening of up states and lengthening of down states of slow oscillations caused by bicuculline in coronal slices from the ferret occipital cortex (Sanchez-Vives *et al.*, 2010). Two spatiotemporal effects were found when GABA_A receptor-mediated inhibition was decreased. First, the temporal profile of oscillations became more regular. Second, the dimension of the patterns of oscillations in both the spatial-amplitude and spatial-frequency domains significantly decreased, which means that the activity pattern of oscillations became simpler and the number of frequency components of the oscillations decreased.

Although the role of GABA_A disinhibition has been extensively explored, the role of GABA_B receptor-mediated inhibition in theta

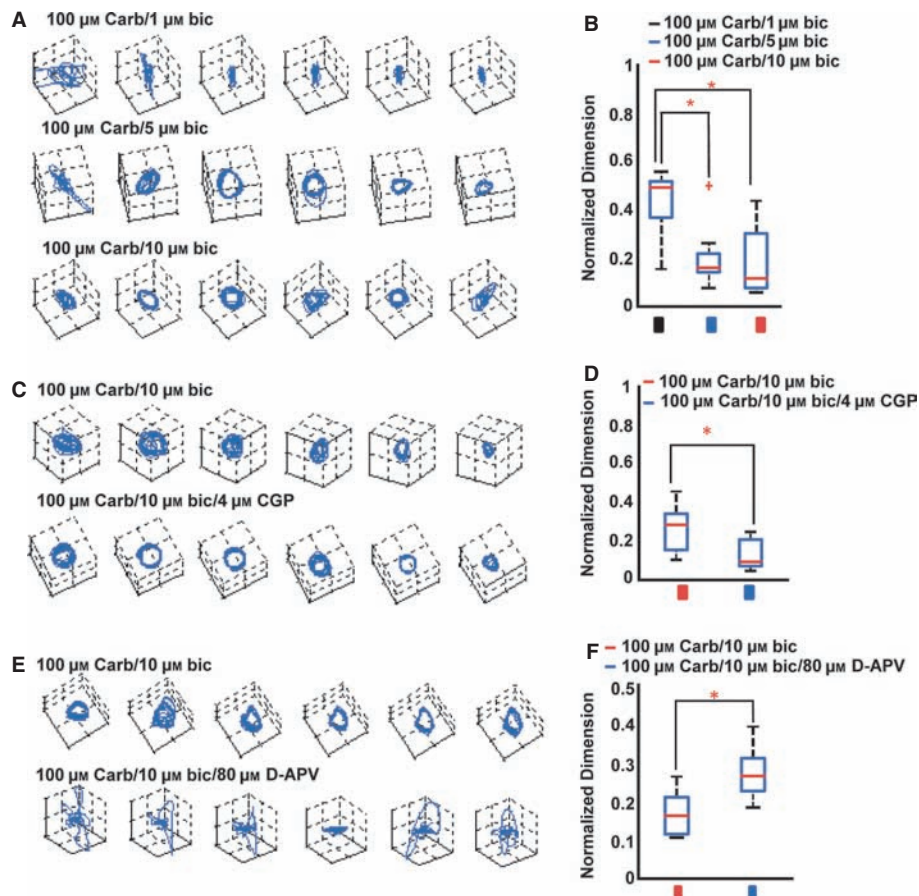


FIG. 4. Dynamical complexity analyses for different conditions. (A) Dynamics from 6-s oscillatory episodes for three bicuculline concentrations are represented by the three rows of trajectory plots. The trajectory plots are formed by plotting the time series of the amplitude of the first three spatial modes (called temporal modes) as the coordinates of the trajectory. Each trajectory plot is derived from a 1 s epoch. Note the simplification of trajectories when 5 and 10 μM bicuculline was added with 100 μM carbachol when compared with 1 μM bicuculline. (B) Box plot for dynamical complexity analysis. Black, blue and red bars represent 1, 5 and 10 μM bicuculline, respectively. Each box bounds the 25 and 75% percentiles [this defines the interquartile range (IQR)]. The red bar inside each box represents the median. Bars above and below the box represent 1.5 times the IQR. The plus sign (+) stands for outlier (defined as outside 1.5 times IQR). One-way ANOVA and Tukey *post hoc* analysis are used to check the significance level in dynamical complexity analysis in B. The 5 μM bicuculline and 10 μM bicuculline groups had significantly lower dimension in spatial-frequency mode than the 1 μM bicuculline group. (C) Trajectory plots for groups with and without GABA_B inhibition. (D) Dynamical complexity analysis for the effect of GABA_B disinhibition. Red and blue bars in D represent groups without and with CGP52432, respectively. CGP52432 significantly decreased dimension in spatial-frequency mode when compared with the group without CGP52432. (E) Trajectory plots for groups without and with NMDA receptor blockade. (F) The effect of NMDA receptor blockade on dynamical complexity. Red and blue bars in F represent groups without and with D-APV, respectively. D-APV significantly increased dimension in spatial-frequency mode. Asterisks in B, D and F indicate significant differences between groups. Carb, carbachol; bic, bicuculline; CGP, CGP52432.

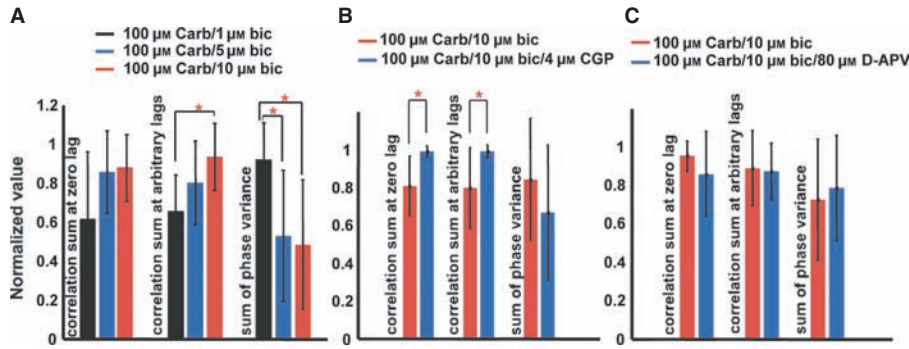


FIG. 5. Synchrony analyses for different conditions. (A) Bar plots show the average normalised values of three parameters for synchrony corresponding to three bicuculline concentrations. Error bars stand for \pm SD. Black, blue and red bars in A represent the 1, 5 and 10 μ M bicuculline groups, respectively. One-way ANOVA and Tukey *post hoc* analysis are used to check the significance level in A. The 10 μ M bicuculline group had a significantly higher cross-correlation sum calculated at arbitrary lags than the 1 μ M bicuculline group; the 5 μ M bicuculline and 10 μ M bicuculline groups had a significantly lower sum of phase variance than the 1 μ M bicuculline group. However, there was no significant difference within groups in the correlation sum calculated at zero lag. (B) Synchrony analysis for the effect of GABA_B disinhibition. Red and blue bars in B represent the 100 μ M carbachol/10 μ M bicuculline group and the 100 μ M carbachol/10 μ M bicuculline/4 μ M CGP52432 group, respectively. CGP52432 significantly elevated the cross-correlation sum at both zero lag and arbitrary lags; however, it did not affect the sum of phase variance when CGP52432 was added. (C) Synchrony analysis for the effect of NMDA receptor blockade. Red and blue bars in C represent the 100 μ M carbachol/10 μ M bicuculline group and the 100 μ M carbachol/10 μ M bicuculline/80 μ M D-APV group, respectively. There was no significant difference in the cross-correlation sum at any lag between groups nor in the sum of phase variance. Asterisks in A and B indicate a significant difference between groups. Carb, carbachol; bic, bicuculline; CGP, CGP52432.

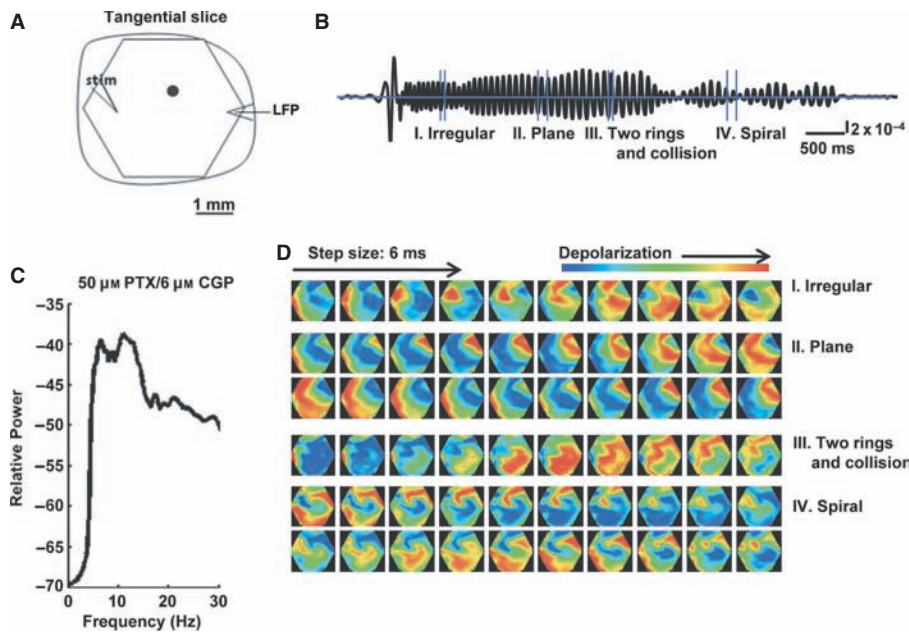


FIG. 6. Oscillations evoked by the combination of picrotoxin (PTX) and CGP52432. (A) Recording arrangement, with stimulation (stim) and local field potential (LFP) electrodes. The signal from one example optical detector (marked as a black filled circle in A) is shown in B. Vertical scale: 2×10^{-4} of resting light intensity. (C) Power spectrum (logarithmic scale) for optical signals averaged from seven slice experiments. The average peak frequencies were at about 6 and 11 Hz. (D) Pattern examples of a 6 s oscillatory episode evoked with 50 μ M PTX/6 μ M CGP52432 in B. These pseudocolor images are displayed at 6 ms intervals between frames. In section III, responses that emerged at two locations in the imaging field developed into two connected rings and collided as the rings propagated.

oscillation remains more elusive (Scanziani, 2000; Buzsáki, 2002; De la Prida *et al.*, 2006). It has been reported that the blockade of GABA_B receptors modulates the amplitude and duration of GABA_A disinhibition-evoked epileptiform bursts in the human cerebral cortex (McCormick, 1989), and helps generate oscillations with bicuculline in the mouse primary motor cortex (Castro-Alamancos & Rigas, 2002). However, it has been difficult to characterise the effects of GABA_B receptor blockade on oscillations evoked by carbachol/bicuculline in coronal neocortical slices (Lukatch & MacIver, 1997) and carbachol-evoked oscillations in hippocampal slices (MacVicar & Tse, 1989). We note that, in Lukatch & MacIver (1997), adding

GABA_B blockade to carbachol- and bicuculline-induced oscillations produced an increase in amplitude and apparent regularization of the oscillations, although they did not comment on these changes. We found that GABA_B disinhibition reliably increased the power of 5–9, 11–17, 22–23 and 25–26 Hz components while shifting the dominant frequency peak toward lower frequencies when compared with carbachol/bicuculline without CGP52432. Combining the effect of bicuculline and CGP52432, more complete GABAergic disinhibition simplifies the cortical dynamics.

It has been reported that, in mouse coronal slices, the blockade of NMDA receptors reduces the power of the 10–15 Hz frequency

component of oscillations evoked by bicuculline/CGP35348, but increases the power of the 15–25 Hz frequency component (Castro-Alamancos & Rigas, 2002). In the coronal cortical slice of rat, the oscillations evoked by carbachol/bicuculline/D-APV intermingle with bursting activity (Lukatch & MacIver, 1997). Our findings of the effects of NMDA blockade are consistent with these previous reports.

At what point are large-amplitude oscillations in the cortex pathological? Our study in the largely deafferented slice cannot say. However, our conjecture is that ‘normal’ likely lies somewhere between the most complex irregular, and the most simple of the large-amplitude oscillations analysed in this report. In a sense, one might view GABA_A and GABA_B receptor-mediated inhibition as helping to maintain the complexity of cortical dynamics. Recent work from Huang *et al.* (2010) suggests that long-range connections to the cortex may serve to break up organised oscillatory waves as we have here studied. Indeed, in previous work of Yuste *et al.* (1997), GABA_A disinhibition served to remove modular architectural boundaries to wave propagation in tangential slices.

The types of coherent and persistent wave formation that we have studied are likely pathological, and the normal connectivity of the cortex may serve to break up such wave dynamics (Huang *et al.*, 2010). Spiral waves in excitable media, biological or chemical (Winfree, 2001), tend to be stable, and mammalian cortices may have sufficient inhibitory connections present to render the lifetime of such rotational waves brief. Whether these periodic dynamics share similarities with epileptic seizure dynamics remains an open question at present, as inhibition appears to play an important role in many types of seizure patterns (see, e.g. Ziburkus *et al.*, 2006, and references therein).

Comparison of paroxysmal discharges in tangential vs. coronal slices

It has been reported that weakening inhibition in interconnected inhibitory networks of the hippocampus may disrupt population rhythmicity (Whittington *et al.*, 1998). In contrast, the present study showed that weakening inhibition of interconnected excitatory networks of the tangential occipital neocortical slice increased the synchronization of activity. The dynamics of brain slices, and their response to pharmacological manipulation, is dependent upon the topology of the slice cut and the residual network anatomy.

In the mouse barrel cortex, paroxysmal discharges evoked by bicuculline in tangential layer IV slices are different in characteristics from those evoked in coronal slices (Fleidervish *et al.*, 1998). The paroxysmal discharges evoked in tangential layer IV slices are completely blocked by an NMDA receptor blocker and are unaffected by the AMPA receptor blocker CNQX, whereas events in coronal slices can only be generated if AMPA receptor-mediated transmission is intact (Golomb & Amitai, 1997). In contrast to the barrel cortex, oscillations evoked by carbachol/bicuculline in rat tangential occipital neocortical slices share many similarities in mechanism with those evoked in coronal neocortical slices. The activation of AMPA receptors is necessary for the generation of propagating oscillations in both coronal neocortical slices (Lukatch & MacIver, 1997) and tangential occipital neocortical slices (the present study), whereas the activation of NMDA receptors modulates oscillation expression in both coronal (Lukatch & MacIver, 1997) and tangential occipital cortical slices.

The mechanism underlying the oscillation dynamics

Slice geometry is critical to the dynamics observed. In the hippocampus, orthogonal networks of dendritic vs. somatic innervating

inhibitory neurons render the dynamics and rhythmicity of transverse vs. longitudinal slices very different (Gloveli *et al.*, 2005). In our experiments, the tangential slice from the middle cortical layers (3–5) is far more isotropic than a coronal slice, and permits the symmetries necessary for coherent traveling wave formation to occur. Another contrast between our findings and that of the oscillations in coronal slices is that our waves propagate readily even at relatively low levels of inhibitory blockade. In a layer-by-layer study of propagation in coronal slices, layer 5 has been shown to be the layer that best supports propagating traveling waves (Telfeian & Connors, 1998). Although the superficial cortical layers (1–3) were important in the generation of stationary oscillations in coronal slices (Lukatch & MacIver, 1997), the middle cortical layers alone can support oscillations when slices are tangentially cut.

Spectral coherency analysis

Membrane voltage changes detected by VSD detectors near the tip of LFP recording electrodes should be most coherent with the LFP. However, there are many sources of noise in VSD signals ranging from photon shot-noise to movement artifacts (Grinvald *et al.*, 1988). In order to analyse data without artifact contamination, spectral coherency analysis was used in the present study to identify a heavily contaminated from a non-contaminated frequency band. We make the assumption that the movement artifact in such optical imaging is independent of any movement-induced neuronal activity, and is additive to the optical signal. We set a conservative criterion to identify a frequency cutoff that separated coherencies between optical channels that could be confirmed by electrical LFP recordings. Below 5 Hz, there were complex results that included many examples of coherencies between optical channels alone without LFP confirmation. We excluded all of these low-frequency results in order to protect against analysing coherent artifacts. Artifacts in VSD imaging of wave dynamics in the brain are common and we offer our strategy as a general approach for artifact reduction in such scenarios. Our suspicion is that the frequency ranges exhibiting substantial movement artifact will differ from one experimental setup to another, subject to vibration-absorbing table characteristics, building vibration, room air circulation movements, etc. We found little evidence for coherency artifacts above 5 Hz in our experiments.

Characterising cortical spatiotemporal dynamics

There is no general strategy to characterise the complexity and similarities of spatiotemporal patterns of brain activity. We have used multivariate metrics of synchronization (Schiff *et al.*, 2005) and mode decompositions (Schiff *et al.*, 2007) to help to classify and characterise such dynamics. In the present study, in addition to standard Fourier frequency decomposition, we used metrics of synchronization and dynamical complexity to characterise the properties of oscillatory waves in the neocortex. We were able to characterise consistent changes (e.g. with adding GABA_B blockade to GABA_A blockade) where other analyses have had some difficulty in observing such effects (Lukatch & MacIver, 1997). How complex the characterisation of oscillatory wave patterns in the cortex needs to be remains an open question. However, the dynamics of the cortex is complex, and our findings suggest that introducing metrics of complexity and synchronization is useful in our efforts to better define the dynamics and pharmacology of cortical waves. Whether this characterisation of network activity, in combination with cellular level electrophysiology, would be an effective way to characterise the

effects of aging, genetic variability or transgenic brain networks remains interesting to consider for future work.

Towards control of cortical oscillations

Although empirical data-driven control strategies can be effective in neuronal systems (Gluckman *et al.*, 2001), we are interested in developing model-based observation and control of neuronal circuitry (Schiff & Sauer, 2008; Schiff, 2010, 2012). Such control systems may be useful for dynamical diseases such as epilepsy and Parkinson's disease, and perhaps might affect the initiation of migraines by modulating spreading depression waves. A VSD experiment in a tangential cortical slice has many advantages for early control experiments. The simultaneous measurement of many different points across the photodiode array permits a multiple input measurement that can increase the observability of any spatiotemporal physical system (Aguirre & Letellier, 2005). The computational overhead for such control systems will be greatly decreased using a purely excitatory neuronal network with GABA_A and GABA_B blockade as shown in these present results, and as demonstrated numerically in Schiff & Sauer (2008). A more difficult challenge for future work will be to develop the technologies to handle multilayered excitatory and inhibitory networks in real time for model-based control. The results of this present study will help to enable the early attempts at this next generation of neuronal controllers.

Supporting Information

Additional supporting information may be found in the online version of this article:

Fig. S1. Traces without low-frequency filtering and including initial stimulation and latent period. (A) Recording arrangement. Signals from two optical detectors (marked as filled circles 1 and 2) and LFPs under three drug conditions are shown in C. The blue dashed lines in traces of C are zero baselines. Vertical scale: 2×10^{-3} of resting light intensity. Horizontal scale: 1 s. The solid blue lines in C mark the stimulus delivery time points. (B) Power spectrum (logarithmic scale) for optical signals during a 6 s episode averaged across all detectors of 10 slice experiments without low-frequency filtering. Note that there was no substantial difference in spectra between 0 and 5 Hz between these different pharmacological conditions. There is a substantial low-frequency component in the raw traces in C that are not affected by the different drug applications. We attribute these low frequencies to likely movement artifact, but some intrinsic signal components may also be present (not reflecting electrical activity). Note the latent period from stimulus to oscillation of about 1 s clearly shown in the LFP traces in C. Carb, carbachol; bic, bicuculline; stim, stimulus.

Fig. S2. Traces without low-frequency filtering with and without CGP52432. (A) Signals from two example optical detectors (marked as 1 and 2 in Fig. S1), along with LFPs, under two drug conditions. Vertical scale: 2×10^{-3} of resting light intensity. Horizontal scale: 1 s. The solid blue lines mark out the stimulus time points. (B) Traces of optical detectors 1 and 2 in A were filtered between 5 and 30 Hz and denoised. Vertical scale: 2×10^{-4} of resting light intensity. (C) Power spectrum (logarithmic scale) for optical signals during a 6 s episode averaged across all detectors of nine slice experiments without low-frequency filtering. The blue dashed lines in traces of A and B are zero baselines. Carb, carbachol; bic, bicuculline; CGP, CGP52432.

Fig. S3. Traces without low-frequency filtering with and without D-APV. (A) Signals from two example optical detectors (marked as 1 and 2 in Fig. S1), along with LFPs, under two drug conditions.

Vertical scale: 2×10^{-3} of resting light intensity. Horizontal scale: 1 s. The vertical solid blue lines mark out the stimulus time points. (B) Traces of optical detectors 1 and 2 in A were filtered between 5 and 30 Hz and denoised. Vertical scale: 2×10^{-4} of resting light intensity. (C) Power spectrum (logarithmic scale) for optical signals during a 6 s episode averaged across all detectors of eight slice experiments without low-pass filtering below 5 Hz. The blue dashed lines in traces of A and B are zero baselines. Carb, carbachol; bic, bicuculline.

Fig. S4. Theta oscillations were eliminated by CNQX. (A) Recording arrangement, with stimulation (stim) and local field potential (LFP) electrodes. Signals from one example optical detector (marked as a black filled circle in (A) with and without CNQX are shown as 6 s traces in B. The blue horizontal lines are zero baselines. Vertical scale: 2×10^{-4} of resting light intensity. (C) Two sections from the temporal data (I and II) in B are displayed as a sequence of pseudocolor images. Note there were no propagating waves during the recording period after CNQX was added.

Movie S1. Ring waves evoked by 1 μ M bicuculline/100 μ M carbachol (AVI).

Movie S2. Plane waves evoked by 5 μ M bicuculline/100 μ M carbachol (AVI).

Movie S3. Spiral waves (AVI).

Movie S4. Ring waves and collisions evoked by 10 μ M bicuculline/100 μ M carbachol (AVI).

Please note: As a service to our authors and readers, this journal provides Supporting Information supplied by the authors. Such materials are peer-reviewed and may be re-organised for online delivery, but are not copy-edited or typeset by Wiley-Blackwell. Technical support issues arising from supporting information (other than missing files) should be addressed to the authors.

Acknowledgements

This work was supported by NIH grant R01MH079502. We are grateful to Weifeng Xu for helpful discussion.

Abbreviations

ACSF, artificial cerebrospinal fluid; CGP52432, 3-[(3,4-dichlorophenyl)methyl] aminopropyl (diethoxymethyl) phosphinic acid; CNQX, 6-cyano-7-nitroquinoxaline-2,3-dione; D-APV, D-(−)-2-amino-5-phosphonopentanoic acid; DMSO, dimethyl sulfoxide; LFP, local field potential; NBQX, 2,3-dioxo-6-nitro-1,2,3,4-tetrahydrobenzo[*f*]quinoxaline-7-sulfonamide; NMDA, N-methyl-D-aspartate; VSD, voltage-sensitive dye.

References

- Aguirre, L.A. & Letellier, C. (2005) Observability of multivariate differential embeddings. *J. Phys. A: Math. Gen.*, **38**, 6311.
- Arieli, A., Sterkin, A., Grinvald, A. & Aertsen, A. (1996) Dynamics of ongoing activity: explanation of the large variability in evoked cortical responses. *Science*, **273**, 1868–1871.
- Bai, L., Huang, X., Yang, Q. & Wu, J.Y. (2006) Spatiotemporal patterns of an evoked network oscillation in neocortical slices: coupled local oscillators. *J. Neurophysiol.*, **96**, 2528–2538.
- Bao, W. & Wu, J.Y. (2003) Propagating wave and irregular dynamics: spatiotemporal patterns of cholinergic theta oscillations in neocortex in vitro. *J. Neurophysiol.*, **90**, 333–341.
- Bendat, J.S. & Piersol, A.G. (1986) *Random Data*. J Wiley & Sons, New York, pp. 484–516.
- Buzsáki, G. (2002) Theta oscillations in the hippocampus. *Neuron*, **33**, 325–340.
- Cappaert, N.L., Lopes da Silva, F.H. & Wadman, W.J. (2009) Spatio-temporal dynamics of theta oscillations in hippocampal-entorhinal slices. *Hippocampus*, **19**, 1065–1077.

- Carlson, G.C. & Coulter, D.A. (2008) In vitro functional imaging in brain slices using fast voltage-sensitive dye imaging combined with whole-cell patch recording. *Nat. Protoc.*, **3**, 249–255.
- Castro-Alamancos, M.A. & Rigas, P. (2002) Synchronized oscillations caused by disinhibition in rodent neocortex are generated by recurrent synaptic activity mediated by AMPA receptors. *J. Physiol.*, **54**, 567–581.
- Coppola, G., Vandenheede, M., Clemente, L.D., Ambrosini, A., Fumal, A., Pasqua, V.D. & Schoenen, J. (2005) Somatosensory evoked high-frequency oscillations reflecting thalamo-cortical activity are decreased in migraine patients between attacks. *Brain*, **128**, 98–103.
- De la Prida, L.M., Huberfeld, G., Cohen, I. & Miles, R. (2006) Threshold behavior in the initiation of hippocampal population bursts. *Neuron*, **49**, 131–142.
- Edden, R.A., Muthukumaraswamy, S.D., Freeman, T.C. & Singh, K.D. (2009) Orientation discrimination performance is predicted by GABA concentration and gamma oscillation frequency in human primary visual cortex. *J. Neurosci.*, **29**, 15721–15726.
- Ermentrout, G.B. & Kleinfeld, D. (2001) Traveling electrical waves in cortex: insights from phase dynamics and speculation on a computational role. *Neuron*, **29**, 33–44.
- Fink, K., Meder, W., Dooley, D.J. & Gothert, M. (2000) Inhibition of neuronal Ca(2+) influx by gabapentin and subsequent reduction of neurotransmitter release from rat neocortical slices. *Br. J. Pharmacol.*, **130**, 900–906.
- Fisahn, A., Pike, F.G., Buhl, E.H. & Paulsen, O. (1998) Cholinergic induction of network oscillations at 40Hz in the hippocampus in vitro. *Nature*, **394**, 186–189.
- Fleidervish, I.A., Binshtok, A.M. & Gutnick, M.J. (1998) Functionally distinct NMDA receptors mediate horizontal connectivity within Layer 4 of mouse barrel cortex. *Neuron*, **21**, 1055–1065.
- Flint, A.C., Maisch, U.S. & Kriegstein, A.R. (1997) Postnatal development of low [Mg²⁺] oscillations in neocortex. *J. Neurophysiol.*, **78**, 1990–1996.
- Geisler, C., Diba, K., Pastalkova, E., Mizuseki, K., Royer, S. & Buzsáki, G. (2010) Temporal delays among place cells determine the frequency of population theta oscillations in the hippocampus. *Proc. Natl. Acad. Sci. USA*, **107**, 7957–7962.
- Gloveli, T., Dugladze, T., Rotstein, H.G., Traub, R.D., Monyer, H., Heinemann, U., Whittington, M.A. & Kopell, N.J. (2005) Orthogonal arrangement of rhythm-generating microcircuits in the hippocampus. *Proc. Natl. Acad. Sci. USA*, **102**, 13295–13300.
- Gluckman, B.J., Nguyen, H., Weinstein, S.L. & Schiff, S.J. (2001) Adaptive electric field control of epileptic seizures. *J. Neurosci.*, **21**, 590–600.
- Golomb, D. & Amitai, Y. (1997) Propagating neuronal discharges in neocortical slices: computational and experimental study. *J. Neurophysiol.*, **78**, 1199–1211.
- Grinvald, A., Frostig, R.D., Lieke, E. & Hildesheim, R. (1988) Optical imaging of neuronal activity. *Physiol. Rev.*, **68**, 1285–1366.
- Huang, X., Troy, W.C., Yang, Q., Ma, H., Laing, C.R., Schiff, S.J. & Wu, J.Y. (2004) Spiral waves in disinhibited mammalian neocortex. *J. Neurosci.*, **24**, 9897–9902.
- Huang, X., Xu, W., Liang, J., Takagaki, K., Gao, X. & Wu, J.Y. (2010) Spiral wave dynamics in neocortex. *Neuron*, **68**, 978–990.
- Jin, W.J., Zhang, R.J. & Wu, J.Y. (2002) Voltage-sensitive dye imaging of population neuronal activity in cortical tissue. *J. Neurosci. Methods*, **115**, 13–27.
- Kleiman-Weiner, M., Beenhakker, M.P., Segal, W.A. & Huguenard, J.R. (2009) Synergistic roles of GABA_A receptors and SK channels in regulating thalamocortical oscillations. *J. Neurophysiol.*, **102**, 203–213.
- Koroleva, V.I., Davydov, V.I. & Roshchina, G.Y. (2009) Properties of spreading depression identified by EEG spectral analysis in conscious rabbits. *Neurosci. Behav. Physiol.*, **39**, 87–97.
- Lam, Y.W., Cohen, L.B., Wachowiak, M. & Zochowski, M.R. (2000) Odors elicit three different oscillations in the turtle olfactory bulb. *J. Neurosci.*, **20**, 749–762.
- Lepousez, G., Mouret, A., Loudes, C., Epelbaum, J. & Viollet, C. (2010) Somatostatin contributes to in vivo gamma oscillation modulation and odor discrimination in the olfactory bulb. *J. Neurosci.*, **30**, 870–875.
- Lukatch, H.S. & MacIver, M.B. (1997) Physiology, pharmacology, and topography of cholinergic neocortical oscillations in vitro. *J. Neurophysiol.*, **77**, 2427–2445.
- Luo, H. & Poeppel, D. (2007) Phase patterns of neuronal responses reliably discriminate speech in human auditory cortex. *Neuron*, **54**, 1001–1010.
- MacVicar, B.A. & Tse, F.W. (1989) Local neuronal circuitry underlying cholinergic rhythmic slow activity in CA3 area of rat hippocampal slices. *J. Physiol.*, **417**, 197–212.
- Mak, J.N. & Wolpaw, J.R. (2009) Clinical applications of brain–computer interfaces: current state and future prospects. *IEEE Rev. Biomed. Eng.*, **2**, 187–199.
- McCormick, D.A. (1989) GABA as an inhibitory neurotransmitter in human cerebral cortex. *J. Neurophysiol.*, **62**, 1018–1027.
- Mitra, P.P. & Pesaran, B. (1999) Analysis of dynamic brain imaging data. *Biophys. J.*, **76**, 691–708.
- Netoff, T.I., Pecora, L.M. & Schiff, S.J. (2004) Analytical coupling detection in the presence of noise and nonlinearity. *Phys. Rev. E Stat. Nonlin. Soft. Matter Phys.*, **69**(1 Pt 2), 017201.
- Palagina, G., Eysel, U.T. & Jancke, D. (2009) Strengthening of lateral activation in adult rat visual cortex after retinal lesions captured with voltage-sensitive dye imaging in vivo. *Proc. Natl. Acad. Sci. USA*, **106**, 8743–8747.
- Pálhalmi, J., Paulsen, O., Freund, T.F. & Hajos, N. (2004) Distinct properties of carbachol- and DHPG-induced network oscillations in hippocampal slices. *Neuropharmacology*, **47**, 381–389.
- Pikovsky, A.S., Rosenblum, M.G. & Kurths, J. (2000) Phase synchronization in regular and chaotic systems. *Int. J. Bifurcat. Chaos*, **10**, 2291–2306.
- Pisani, A., Bonsi, P., Catania, M.V., Giuffrida, R., Morari, M., Centonze, D., Bernardi, G., Kingston, A.E. & Calabresi, P. (2002) Metabotropic glutamate 2 receptors modulate synaptic inputs and calcium signals in striatal cholinergic interneurons. *J. Neurosci.*, **22**, 6176–6185.
- Precht, J.C., Cohen, L.B., Pesaran, B., Mitra, P.P. & Kleinfeld, D. (1997) Visual stimuli induce waves of electrical activity in turtle cortex. *Proc. Natl. Acad. Sci. USA*, **94**, 7621–7626.
- Raghavachari, S., Kahana, M.J., Rizzuto, D.S., Caplan, J.B., Kirschen, M.P., Bourgeois, B., Madsen, J.R. & Lisman, J.E. (2001) Gating of human theta oscillations by a working memory task. *J. Neurosci.*, **21**, 3175–3183.
- Reimer, J. & Hatsopoulos, N.G. (2010) Periodicity and evoked responses in motor cortex. *J. Neurosci.*, **30**, 11506–11515.
- Richter, D., Luhmann, H.J. & Kilb, W. (2010) Intrinsic activation of GABA receptors suppresses epileptiform activity in the cerebral cortex of immature mice. *Epilepsia*, **51**, 1483–1492.
- Rizzuto, D.S., Madsen, J.R., Bromfield, E.B., Schulze-Bonhage, A., Seelig, D., Aschenbrenner-Scheibe, R. & Kahana, M.J. (2003) Reset of human neocortical oscillations during a working memory task. *Proc. Natl. Acad. Sci. USA*, **100**, 7931–7936.
- Rubino, D., Robbins, K.A. & Hatsopoulos, N.G. (2006) Propagating waves mediate information transfer in the motor cortex. *Nat. Neurosci.*, **9**, 1549–1557.
- Sanchez-Vives, M.A. & McCormick, D.A. (2000) Cellular and network mechanisms of rhythmic recurrent activity in neocortex. *Nat. Neurosci.*, **3**, 1027–1034.
- Scanziani, M. (2000) GABA spillover activates postsynaptic GABA_B receptors to control rhythmic hippocampal activity. *Neuron*, **25**, 673–681.
- Schiff, S.J. (2010) Towards model-based control of Parkinson's disease. *Philos. Transact. A Math. Phys. Eng. Sci.*, **368**, 2269–2308.
- Schiff, S.J. (2012) *Neural Control Engineering*. MIT Press, Cambridge.
- Schiff, S.J. & Sauer, T. (2008) Kalman filter control of a model of spatiotemporal cortical dynamics. *J. Neural Eng.*, **5**, 1–8.
- Schiff, S.J., Sauer, T., Kumar, R. & Weinstein, S.L. (2005) Neuronal spatiotemporal pattern discrimination: the dynamical evolution of seizures. *Neuroimage*, **28**, 1043–1055.
- Schiff, S.J., Huang, X. & Wu, J.Y. (2007) Dynamical evolution of spatiotemporal patterns in mammalian middle cortex. *Phys. Rev. Lett.*, **98**, 178102.
- Senseman, D.M. & Robbins, K.A. (1999) Modal behavior of cortical neural networks during visual processing. *J. Neurosci.*, **19**, RC3 1–7.
- Sun, W. & Dan, Y. (2009) Layer-specific network oscillation and spatiotemporal receptive field in the visual cortex. *Proc. Natl. Acad. Sci. USA*, **106**, 17986–17991.
- Tancredi, V., Biagini, G., D'Antuono, M., Louvel, J., Pumain, R. & Avoli, M. (2000) Spindle-like thalamocortical synchronization in a rat brain slice preparation. *J. Neurophysiol.*, **84**, 1093–1097.
- Telfeian, A.E. & Connors, B.W. (1998) Layer-specific pathways for the horizontal propagation of epileptiform discharges in neocortex. *Epilepsia*, **39**, 700–708.
- Towers, S.K., LeBeau, F.E., Gloveli, T., Traub, R.D., Whittington, M.A. & Buhl, E.H. (2002) Fast network oscillations in the rat dentate gyrus in vitro. *J. Neurophysiol.*, **87**, 1165–1168.

- Treiman, D.M. (2001) GABAergic mechanism in epilepsy. *Epilepsia*, **42**(Suppl. 3), 8–12.
- Whittington, M.A., Traub, R.D., Faulkner, H.J., Jeferys, J.G. & Chettiar, K. (1998) Morphine disrupts long-range synchrony of gamma oscillations in hippocampal slices. *Proc. Natl. Acad. Sci. USA*, **95**, 5807–5811.
- Williams, J.H. & Kauer, J.A. (1997) Properties of carbachol-induced oscillatory activity in rat hippocampus. *J. Neurophysiol.*, **78**, 2631–2640.
- Winfree, A.T. (2001). *The Geometry of Biological Time*. Springer-Verlag, New York.
- Worrell, G.A., Parish, L., Cranstoun, S.D., Jonas, R., Baltuch, G. & Litt, B. (2004) High-frequency oscillations and seizure generation in neocortical epilepsy. *Brain*, **127**, 1496–1506.
- Wu, J.Y., Guan, L., Bai, L. & Yang, Q. (2001) Spatiotemporal properties of an evoked population activity in rat sensory cortical slices. *J. Neurophysiol.*, **86**, 2461–2474.
- Xu, W., Huang, X., Takagaki, K. & Wu, J.Y. (2007) Compression and reflection of visually evoked cortical waves. *Neuron*, **55**, 119–129.
- Yuste, R., Tank, D.W. & Kleinfeld, D. (1997) Functional study of the rat cortical microcircuitry with voltage-sensitive dye imaging of neocortical slices. *Cereb. Cortex*, **7**, 546–558.
- Ziburkus, J., Cressman, J.R., Barreto, E. & Schiff, S.J. (2006) Interneuron and pyramidal cell interplay during in vitro seizure-like events. *J. Neurophysiol.*, **95**, 3948–3954.

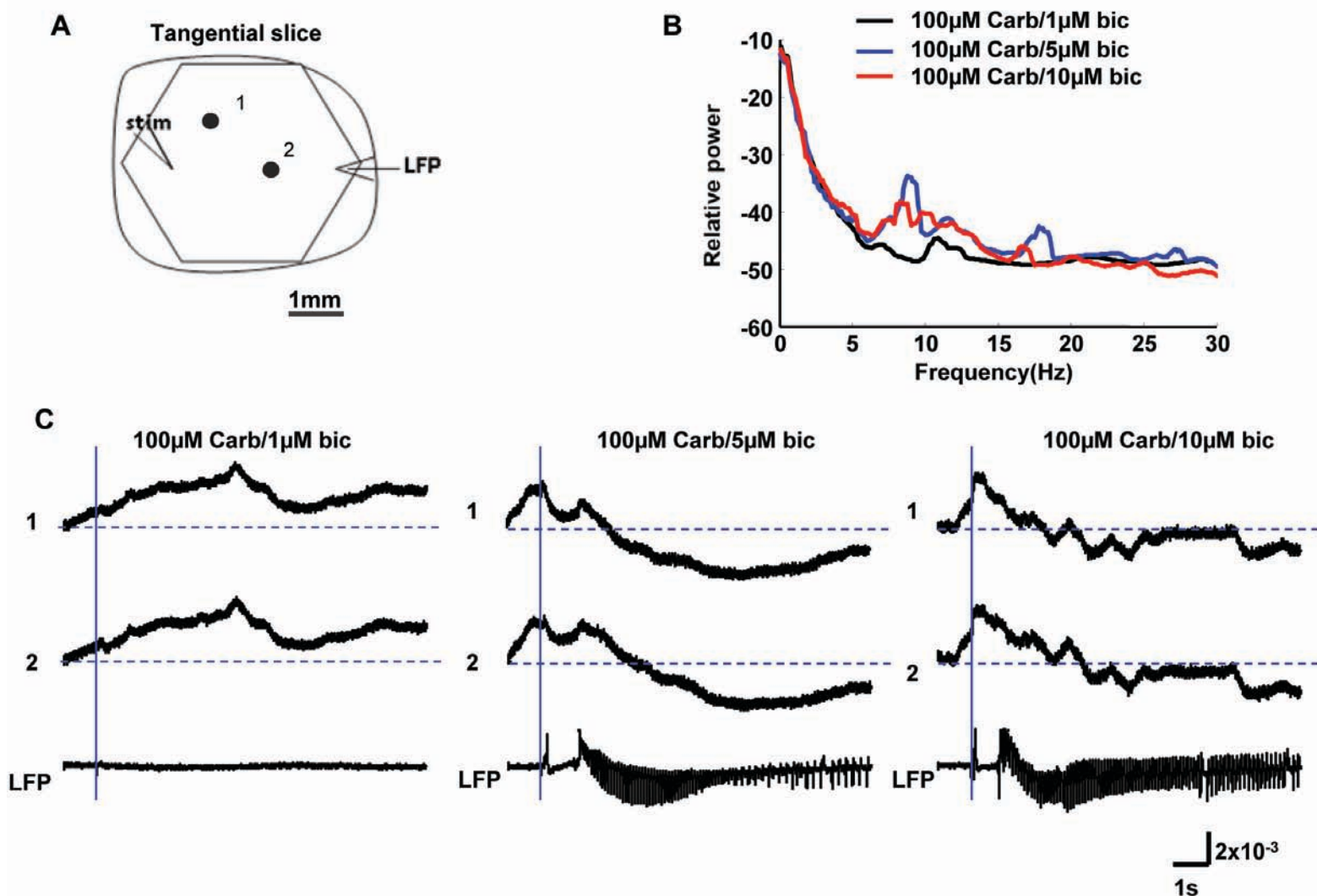


FIG. S1. Traces without low frequency filtering and including initial stimulation and latent period. (A) Recording arrangement. Signals from two optical detectors (marked as 1 and 2 filled circles) and local field potentials (LFPs), under 3 drug conditions are shown in (C). The blue dashed lines in traces of C are zero baselines. Vertical scale: 2×10^{-3} of resting light intensity. Horizontal scale: 1second. The solid blue lines in C mark the stimulus delivery time points. (B) Power spectrum (logarithmic scale) for optical signals during a 6-second episode averaged across all detectors of 10 slice experiments without low frequency filtering. Note that there was no substantial difference in spectra between 0-5 Hz between these different pharmacological conditions. There is substantial low frequency component in the raw traces in C that are not affected by the different drug applications. We attribute these low frequencies to likely movement artifact, but some intrinsic signal components may be present as well (not reflecting electrical activity). Note the latent period from stimulus to oscillation of about 1s clearly shown in the LFP traces in C. Carb: carbachol; bic: bicuculline ; stim: stimulus.

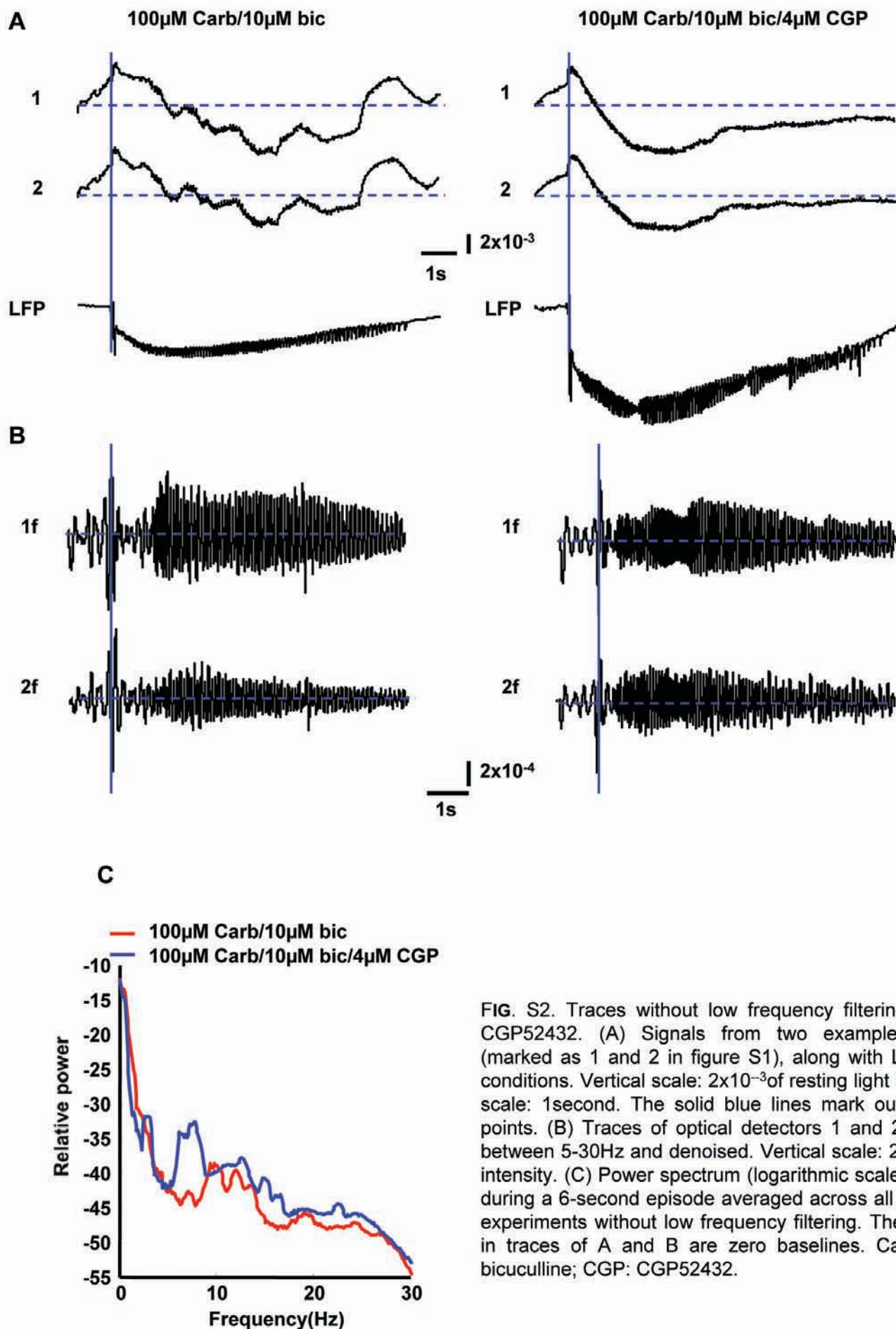
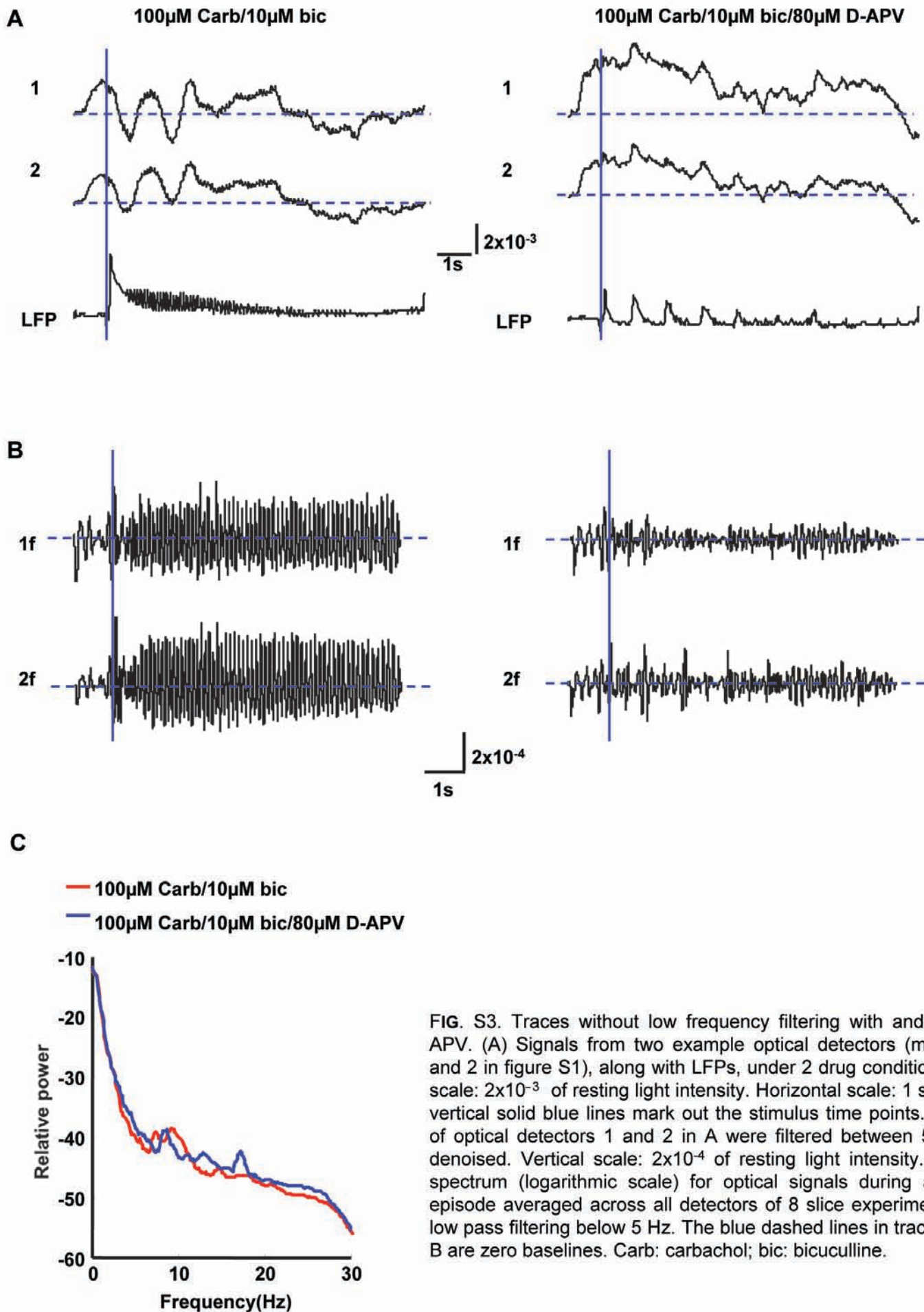


FIG. S2. Traces without low frequency filtering with and without CGP52432. (A) Signals from two example optical detectors (marked as 1 and 2 in figure S1), along with LFPs, under 2 drug conditions. Vertical scale: 2×10^{-3} of resting light intensity. Horizontal scale: 1 second. The solid blue lines mark out the stimulus time points. (B) Traces of optical detectors 1 and 2 in A were filtered between 5-30 Hz and denoised. Vertical scale: 2×10^{-4} of resting light intensity. (C) Power spectrum (logarithmic scale) for optical signals during a 6-second episode averaged across all detectors of 9 slice experiments without low frequency filtering. The blue dashed lines in traces of A and B are zero baselines. Carb: carbachol; bic: bicuculline; CGP: CGP52432.



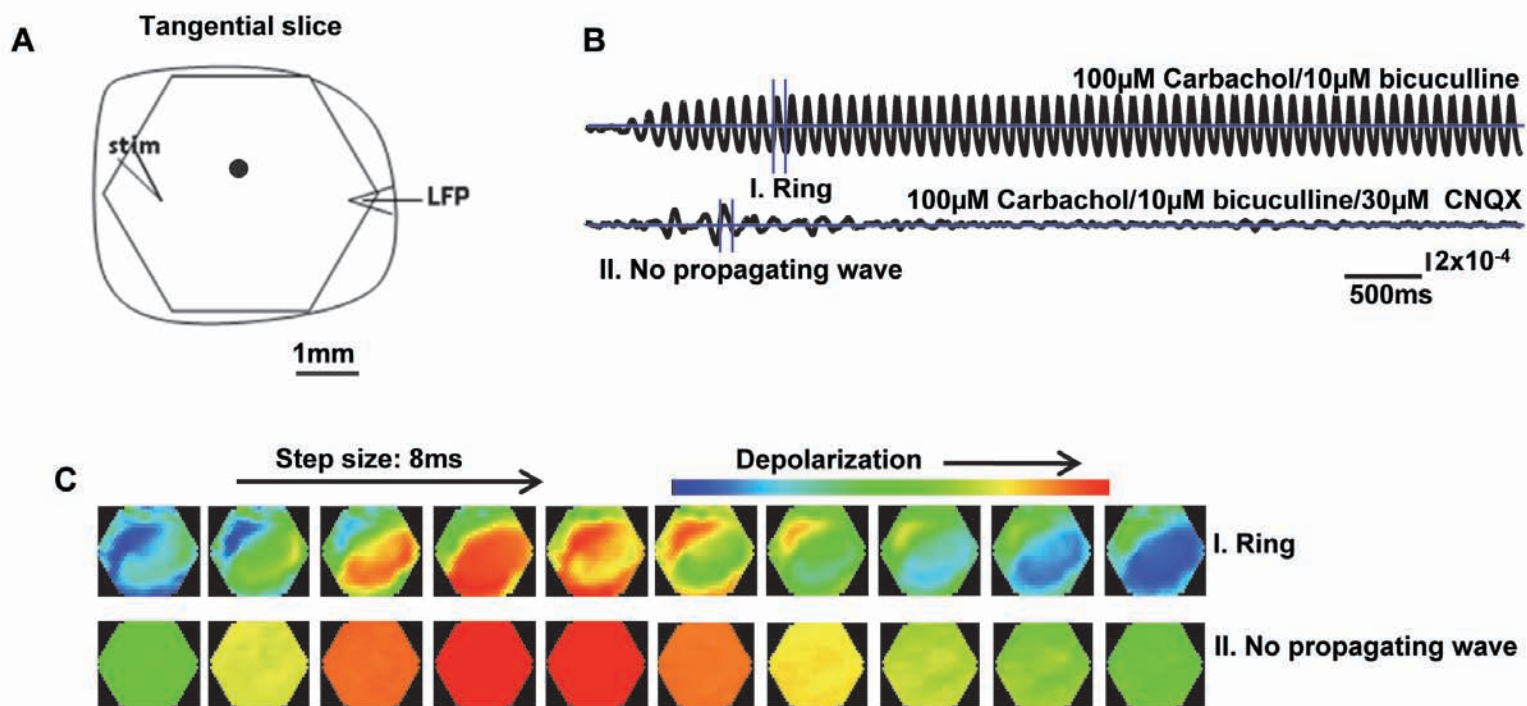


FIG. S4. Theta oscillations were eliminated by CNQX. (A) Recording arrangement. Signals from one example optical detector (marked as a black filled circle in A) with and without CNQX are shown as 6-second traces in (B). The blue horizontal lines are zero baselines. Vertical scale: 2×10^{-4} of resting light intensity. (C) Two sections from the temporal data (I and II) in B are displayed as a sequence of pseudocolor images. Note there were no propagating waves during the recording period after CNQX was added.